ELSEVIER

Theoretical and Applied Fracture Mechanics 31 (1999) 1–17

theoretical and applied fracture mechanics

On-line analysis of hydro-abrasive erosion of pre-cracked materials by acoustic emission

A.W. Momber [a,*,1], R.S. Mohan [b], R. Kovacevic [c]

[a] *WOMA Apparatebau GmbH, P.O. Box 141820, D-47208 Duisburg, Germany*
[b] *The University of Tulsa, Department of Mechanical Engineering, Tulsa, OK, USA*
[c] *Southern Methodist University, Department of Mechanical Engineering, Dallas, TX, USA*

Abstract

Acoustic Emission (AE) sensing technique is used as a tool for on-line monitoring of hydro-abrasive erosion (HAE) of pre-cracked multiphase materials. As reference materials, five types of concrete materials were used for the experimental study. Compression tests were performed to determine the mechanical properties and the failure behavior of these materials. Erosion parameters, such as abrasive particle velocity, local exposure time, and abrasive mass flow rate were varied during the experiments and AE-signals were acquired. The trends exhibited by the time domain and frequency domain AE-signals with change in process parameters and material properties were analyzed. The results indicate that acoustic emission signal is capable of revealing the different material removal mechanisms occurring in pre-cracked multiphase materials when subjected to hydro-abrasive erosion. Visualization studies performed on the erosion site provide more insight into the physics of the process and verify the observations made from the AE-signals. Finally, it is concluded that due to its capability to quantify the amount of material removed, AE_{RMS} could be considered as a parameter for monitoring the material removal process.

1. Introduction

As a new manufacturing process, hydro-abrasive erosion (HAE) has been very effective for cutting difficult-to-machine materials. The tool that is used for the material removal process is a high-speed abrasive-water jet. From the point of view of jet generation, the technique could be categorized as injection jets or suspension jets. Injection jets are the most commonly used type for practical applications. An injection jet is formed by accelerating small abrasive particles through contact with a high velocity plain water jet. The velocity of the plain water jet can be estimated by applying the Bernoulli's law of pressure constancy,

$$v_w = \mu\sqrt{\frac{2p}{\rho_w}}. \quad (1)$$

The mixing of abrasives, water and air takes place in a mixing chamber, whereas the acceleration process occurs in a focus tube. The abrasive particles leave this focus at velocities of several hundred meters per second. The abrasive particle velocity can be approximated by assuming a simple momentum balance in the mixing chamber.

* Corresponding author. Tel.: +49-2065-304 380; fax: +49-2065-304 200.

[1] Visiting Scholar at The Southern Methodist University, Department of Mechanical Engineering, Dallas, TX, USA.

0167-8442/99/$ – see front matter
PII: S0167-8442(98)00062-7

Neglecting the mass flow rate of the air which is sucked with the abrasive material, the abrasive particle velocity is,

$$v_A = \varphi \frac{v_w}{1 + (\dot{m}_A/\dot{m}_w)}. \quad (2)$$

In Eqs. (1) and (2), the parameters μ and φ are momentum transfer coefficients of water and abrasive acceleration, respectively.

Hydro-abrasive erosion (HAE) is one possible solution for the manufacture of high quality workpieces of brittle multiphase materials, such as ceramics, high-strength concrete, and composite materials, of special shapes and forms. Due to their tendency for microcracking, these materials are considered to be hard to machine by conventional tools. Despite this need, the number of serious investigations on the machinability of this type of materials by HAE is comparatively low.

Kim et al. [1] investigated ceramic stock removal using HAE. They conducted piercing and cutting experiments on alumina ceramics and discussed the influence of several process parameters on the piercing process. They demonstrated that the HAE could be effectively used to machine even high-strength ceramics. Neusen et al. [2] carried out cutting experiments on aluminum–silicon carbide and observed smearing of aluminum on the cut surface as well as embedding of fractured abrasive particles. They identified wear by individual abrasive particles as one of the micro mechanisms of material removal. Later, Freist et al. [3] reported about the application of HAE for three-dimensional machining (milling) of alumina ceramics. This work included the development of a kerf geometry model as well as a limited parameter study. Hamatani and Ramulu [4] made use of HAE for piercing of ceramics. They found random damage on the top surface of the pierced holes as well as non-linear hole tapers. They also detected a notable increase in the target temperature and concluded that HAE-machining of ceramics may not be totally free of thermal effects.

Zeng and Kim [5] conducted SEM-observations to evaluate the behavior of sintered aluminum oxide ceramics subjected to HAE under different jet impingement angles. They observed intergranular cracking and plastic flow as the two major material removal mechanisms. The intergranular fracture dominates the material removal mode in the normal impingement, whereas for small angle impact, plastic flow also has equal significance. In an advanced investigation [6], they developed a material removal model as well as a kerf cutting model for brittle materials processed by HAE. To verify their model, they carried out cutting experiments under different process conditions, such as different pump pressures, traverse rates, abrasive mass flow rates, and focus diameters. Nevertheless, it was found [7] that intergranular fracture dominates the removal process only in materials that are characterized by a low-strength matrix and fine inclusion grains. For materials with comparatively high matrix strength and coarse inclusions, cracking occurs through the matrix as well as through the inclusion grains and the failure is dominated by transgranular fracture. The quantitative model for cutting brittle materials by HAE developed by Zeng and Kim [6] is used in this study for discussing the erosion behavior of the investigated materials. Ramulu et al. [8] machined composite ceramics by HAE at shallow impacting angles and observed erosion by microcutting in the matrix whereas the inclusions were removed by the shoveling action of the incoming jet.

In contrast to the kinetic process discussions, Kahlman et al. [9], who observed that the formation of high localized temperatures (about 1280°C) on the surfaces of ceramics during the HAE-process, introduced thermal spalling failure of ceramic materials. They assumed that cooling by the water flow creates local stress fields. Based on SEM-photographs and wear volume measurements, these references defined the thermal shock resistance, R_S, as the main resistance parameter against HAE and defined a machining limit for ceramics at $R_S = 15$ W/mm. Above this value the material removal rapidly decreases.

Hochheng and Cheng [10] reported about volume removal studies on aluminum oxide and silicon nitride ceramics. In their study, they investigated the influence of several process parameters, such as pump pressure and abrasive

mass flow rate, on material removal rate and surface quality. Nevertheless, no attempt was made to discuss the presented experimental results in terms of basic material removal mechanisms.

Momber et al. [11] investigated the behavior of refractory ceramics machined by HAE. Through SEM-studies they found that the material removal mode changes from predominantly transgranular fracture in the upper wall region to a combination of inter-granular fracture and matrix removal, in the lower region of the wall. This observation was explained by the loss of the abrasive particle kinetic energy during the erosion process as theoretically treated in Refs. [12,13]. They found that the machinability of ceramic materials by HAE is influenced by their capability to plastically deform. In a unique contribution, Momber and Kovacevic [7] could show that similarities exist in the behavior of pre-cracked materials during the conventional compression test and during the HAE-machining. For this reason, Momber and Kovacevic [14] found surprisingly good agreement between the depth of cut in concrete materials and their mechanical properties, such as compressive strength and the Young's modulus.

Despite these studies, the knowledge about the behavior of pre-cracked multiphase materials subjected to HAE is just preliminary. One major reason could be that 'off-line' methods, such as SEM-studies, geometry measurements on the erosion site, and surface topography measurements are used for the analysis and observation of the process. These methods require an interruption of the material removal process to obtain suitable information. These 'post-process' results are then linked to the real process. Therefore, the application of 'on-line' methods, which allow a direct real-time observation of the microscopic and macroscopic features of the material removal mechanism, may provide additional information about the HAE-process. Experimental on-line methods which could be applied to HAE are photoelasticity [15], jet and workpiece reaction force measurements [16], and AE sensing technique.

AE-technique was used spontaneously in the field of water jet cutting [17], solid particle erosion [18], and abrasive water jet cutting [19]. The first systematic investigation of AE-signals generated during the HAE-machining process was performed in Refs. [20,21]. Using advanced signal processing techniques, these authors detected functional relationships between the AE-signals acquired during the cutting of metals by HAE on one hand, and the erosion depth and the energy dissipated in the specimen on the other. They also found that AE-technique may be a useful tool for HAE material removal process monitoring and control for metals.

Acoustic emission, in the sense of this paper, refers to elastic waves produced by microscopic deformations occurring in materials, as they are stressed. It contains part of the elastic energy released during deformation. Sometimes called stress wave emissions, acoustic emissions are associated with dislocation movements, crack growth, deformations and other mechanisms. These are sources which are related to the eroded *materials*. Other types of sources, such as pressure pulses, turbulence, and cavitation, depend on the *fluid dynamics* of the process.

2. Experimental setup and procedure

2.1. Experimental setup

The experimental setup consists of an AWJ cutting system, AE-sensor, pre-amplifier, A/D converter, AE monitoring system, PC/AT with suitable software and workpiece. The AWJ cutting system used for conducting the experiment consists of a high-pressure intensifier pump, AWJ cutting head, abrasive metering and delivery system, abrasive hopper with garnet as abrasive, catcher tank, and X–Y–Z positioning system controlled by a CNC controller. A schematic of the experimental setup is shown in Fig. 1.

The generated AE-signals were detected and processed by Model AET 5500 Acoustic Emission Monitoring System which consists of AET 5500 mainframe (signal processing unit), graphics terminal (interface, data storage and display) and the accessories (sensors, pre-amplifiers etc.). When an acoustic emission caused by an induced stress occurs in a test specimen, the sensors (resonant

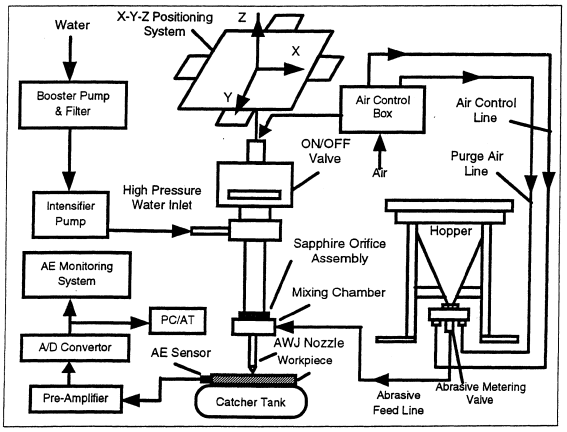

Fig. 1. Experimental setup.

frequency 2 MHz), fixed on top of the specimen, convert this acoustic emission wave into a voltage signal which is amplified by the pre-amplifier and sent to the mainframe (16-bit microprocessor) for post-processing. The distance between cut/kerf and sensor was between 5 and 90 mm. The sensor was fixed on the samples with a water resistant epoxy-adhesive. The raw signal from the AE-monitoring system was acquired at 1 MHz sampling frequency (with a gain of 5.0) using a suitable PC-based data acquisition system for spectrum analysis. Each data set consists of 1024 discrete time domain points. Five data sets of the Fast Fourier Transform (FFT) of the time domain signals acquired under the same experimental conditions were averaged and the representative signal was obtained for future analysis.

The HAE-parameters, namely abrasive particle velocity, local exposure time, and abrasive mass flow rate were varied and linear cuts were made on the workpieces. The abrasive particle velocity was calculated by Eqs. (1) and (2). The momentum transfer parameters in these equations were taken from Ref. [22]. The local exposure time was estimated by

$$t_{\mathrm{E}} = \frac{d_{\mathrm{F}}}{v_{\mathrm{T}}}. \tag{3}$$

The abrasive mass flow rate was varied by a micro-screw in a special metering device. After cutting, the dimensions of the generated cuts, such as depth of cut, cut width, and cut length, were measured as average values of five measurements. The process parameters of these experiments are shown in Table 1. The 14 experimental conditions in Table 1 were repeated for each workpiece material.

For all 70 parameter combinations, a theoretical depth of cut has been calculated based on the model in Ref. [6]. These values are then compared with the experimentally estimated depth values and discussed in terms of deviation between the model and experiment.

2.2. Test materials

For the investigation, five different concrete mixtures (#1–#5) were created and six specimens of each mixture were manufactured. The mechanical properties of these materials were influenced by changing the water–cement ratio and the aggregate fineness (Table 2). The strength of the cement matrix as well as the average inclusion diameter were increased in the order from #1–#5. After mixing and placing, these mixtures were cured and hardened for 28 days under water. After hardening, three cylindrical specimens of each mixture were tested to estimate the mechanical properties, such as compressive strength, Young's modulus, absorbed fracture energy, and crack velocity. The dimensions of the cylindrical specimen used for these tests were 30.8 cm in length and 15.24 cm in diameter. The compressive strength was measured according to the ASME Standard C 39, and the Young's modulus was estimated as the static chord modulus according to the ASTM Standard C 469.

The energy absorbed during the compression fracture test was approximated as follows. The stress–strain curves of the materials were determined by loading and unloading the strain-gauge equipped specimen 11-times and then expressed by a parabolic regression. The area enveloped by the stress–strain curve and the ultimate strain was then calculated by integrating,

$$E_{\mathrm{AB}} = \int_0^{\varepsilon_{\mathrm{ult}}} \left[A \cdot (\varepsilon - \varepsilon_{\mathrm{ult}})^2 + \sigma_{\mathrm{ult}} \right] \mathrm{d}\varepsilon. \tag{4}$$

Table 1
Experimental process parameters

Part (a) Constant parameters

Abrasive waterjet cutting	
Abrasive material	Garnet
Abrasive mesh size	#36 ($d_P = 425$ μm)
Abrasive particle shape	angular (random)
Orifice material	Sapphire
Orifice diameter	0.457 mm
Mixing nozzle length	88.9 mm
Mixing nozzle diameter	1.27 mm
Stand-off distance	6.00 mm
Method of feed	suction
Abrasive condition	dry
Jet impact angle	90 degrees
Workpiece details	
Material	Mixtures # 1–# 5
Material thickness	310 mm
Length of cut	50–80 mm

Part (b) Variable parameters

	Erosion conditions		
Cut No.	Pressure [MPa]	Traverse rate [mm/s]	Abrasive mass flow rate [g/s]
1	100	4.0	7.41
2	150	4.0	7.41
3	200	4.0	7.41
4	250	4.0	7.41
5	300	4.0	7.41
6	350	4.0	7.41
7	200	2.0	7.41
8	200	6.0	7.41
9	200	8.0	7.41
10	200	12.0	7.41
11	200	4.0	6.12
12	200	4.0	10.58
13	200	4.0	14.32
14	200	4.0	19.00

Table 2
Composition and mechanical properties of the specimens

Concrete mixture	Aggregate [a]/ cement [b]	Sand [c] [%]	Water/cement	Y_M [GPa]	σ_M [MPa]	E_{AB} [MJ/m^3]	ρ_M [kg/m^3]
#1	2.24	80	0.85	10.7	4.0	1.5	1962
#2	2.51	70	0.71	24.1	12.5	7.9	2107
#3	2.13	60	0.45	33.0	27.1	27.0	2107
#4	2.25	50	0.38	34.3	34.2	40.9	2135
#5	2.26	40	0.32	42.3	47.6	72.8	2343

[a] coarse limestone aggregates (maximum grain size 19 mm) and river sand (maximum grain size 4.7 mm).
[b] Portland Cement, Type I.
[c] river sand (maximum grain size 4.7 mm).

In order to obtain information about the mechanical behavior of the different type of materials used in this study, the standard compression test was combined with an analysis of the material fragments which remained after the specimen failure. These fragments were collected and classified into two groups as suggested by Momber [23]. The first group contained the main debris from the top and the bottom of the specimen which are usually cone-shaped (see Fig. 2), whereas the second group contained the fine-grained material from the periphery of the specimen. These grain collections were investigated by sieve analysis.

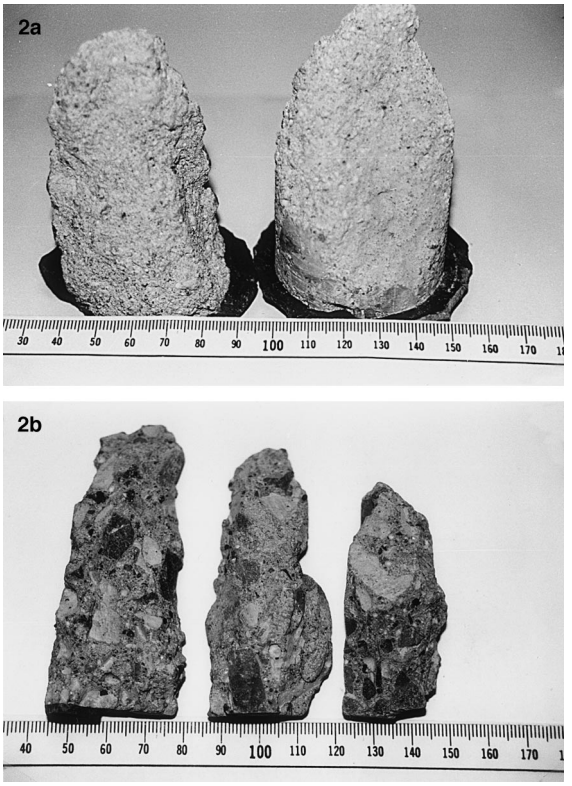

Fig. 2. Fragments generated during the compression tests of the concrete specimens: (a) Fragments (conical) generated during the compression test of concrete #1; (b) fragments (splitting) generated during the compression test of concrete #5 (several broken inclusion grains are shown).

3. Experimental results

3.1. Compression tests

The mechanical properties obtained by the standard compression tests are listed in Table 2. It can be seen that the mechanical properties increase with the number of the material mixture. The concrete #1 exhibits comparatively low values and concrete #5 high values.

The results obtained from the analysis of the fragments of the cylinder compression tests are discussed in detail in Ref. [23]. It was found that the concrete mixtures with the low mechanical properties (concrete #1–#3) are characterized by a cone-type failure with a high degree of intergranular fracture on the cone surfaces. This failure mode is illustrated in Fig. 2(a) showing two cones generated during the testing of concrete #1. In contrast, the high-strength concrete mixtures (concrete #4 and #5) showed a splitting mode failure, mainly by transgranular fracture. This is illustrated in Fig. 2(b), which shows the fragments of the cylinder specimen made from concrete #5. It can be seen that the number of fragments is higher. Also, the broken aggregate grains can be clearly distinguished. As the latter failure mode requires more energy due to the high specific surface energies of the fractured aggregate grains, these observations are in good agreement with the measured absorbed fracture energies (Table 2). It was also found that the fine grained material generated during the compression test has characteristic features. Most significantly, the average particle diameter of the fine grained material increases with an increase in the mechanical properties of the material. Also, with increasing material strength, the shape of the grains changed from almost spherical (concrete #1) to sharp edged (concrete #5), indicating different failure behaviors. The results obtained from the compression test suggest that with increasing strength properties, the failure mode changes from a ‘crumble’ intergranular fracture for low-strength materials to a ‘spalling’ transgranular fracture for high-strength materials.

3.2. Cutting experiments

The influence of the investigated process parameters on the erosion depth in the materials is illustrated in Fig. 3. Fig. 3(a) shows the influence of the *abrasive particle velocity*. Here, two interesting features could be noticed. First, the relationship is highly non-linear with a decreasing trend at higher particle velocities, indicating that the material removal process is less efficient at higher velocity levels. Second, a critical abrasive particle velocity, v_{THR}, could be noticed at the intersection of the velocity axis and the depth function which describes the minimum impact velocity required to erode the material. A similar parameter is also known from dry solid particle erosion

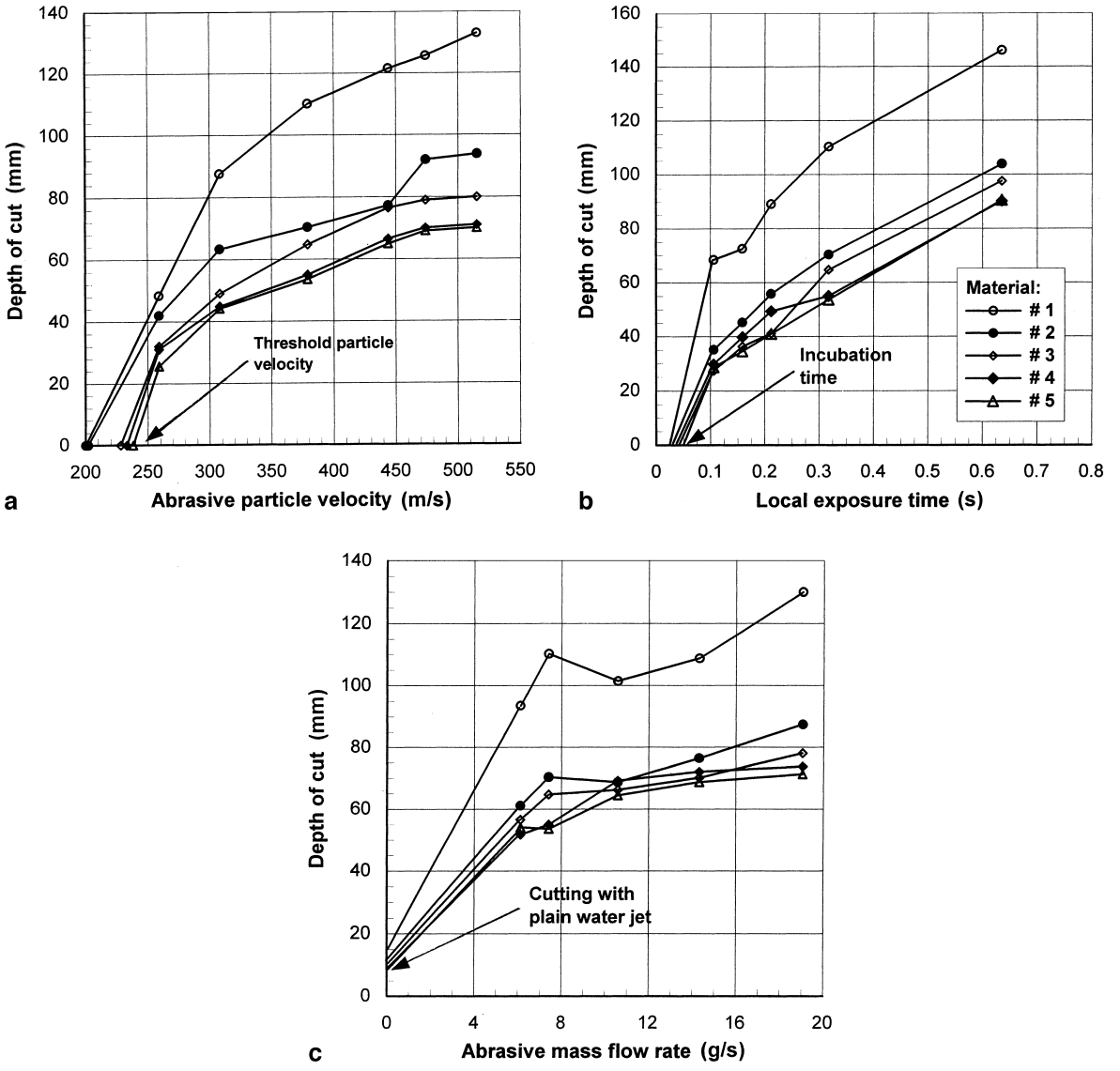

Fig. 3. Process parameter influence on the depth of cut in the investigated materials: (a) Abrasive particle velocity; (b) local exposure time; (c) abrasive mass flow rate.

[24] and is considered as the material 'threshold velocity'. In the present case, the values are between 200 and 240 m/s. It can be seen that this parameter increases with an increase in the material strength properties. But interestingly, even if two materials are having almost identical threshold velocities (concrete #1 and #2), they will behave quite differently once the erosion process is introduced and as they are attacked by higher velocities.

The influence of the *local exposure time* on the erosion depth is shown in Fig. 3(b). Similar to Fig. 3(a), a threshold value could be noticed. This 'incubation time' illuminates the fact that a certain number of impacting particles may be required to introduce the erosion process. The material removal process starts once this value is exceeded. The incubation periods are located in a narrow range between 0.025 and 0.05 s. The relationships in Fig. 3(b) are non-linear and the progress drops at long exposure times. As the results show, the erosion process is very sensitive in the range of short exposure times. In this range ($t_E < 0.1$ s) just small variations in the exposure time yield significant changes in the depth of cut. Interestingly, the initial slopes of the functions depend on the material type. It is very high for the low-strength concrete #1 and decreases as the concrete strength increases. Obviously, low-strength materials are less sensitive to damping effects in this stage. Later, the slopes of the different materials are almost equal. For very long exposure times, it can be assumed that the cutting process has some similarities with the piercing process. In particular, damping processes may play a significant role in determining the material removal process. Therefore, it is assumed by several authors that the depth of cut in a material has a constant value for long exposure times. It can be assumed that the function may approximate this maximum possible depth. Again, one feature could be observed: although the incubation times for all mixtures are very close together, the materials show a very different erosion resistance. Obviously, the different conditions for damping, friction and other energy consuming processes are not established during the incubation period.

Fig. 3(c) illustrates the influence of the *abrasive mass flow rate* on the cutting process. As the materials could be eroded by plain water jets the functions do not start at zero. For low abrasive mass flow rates ($m_A < 6$ g/s) the erosion depth increases rapidly with an increase in the abrasive mass flow rate. For the investigated flow rate range, the influence of the abrasive mass flow rate on the erosion depth is weak. The reason may be that for the given process condition, including particle mixing and material removal, a critical abrasive mass flow rate exists. Beyond this critical flow rate, the number of abrasives is too large for efficient acceleration and cutting. This leads to loss of efficiency in the mixing chamber as well as on the erosion site due to friction, damping, particle collision, and particle fragmentation. Therefore, a further increase in the abrasive flow rate will not significantly increase the depth of cut. The frequency of impacting abrasive particles has been calculated by an approximation method; it is between 180 and 460 kHz. Interestingly, concrete #1 does not follow this trend consequently. As the abrasive mass flow rate exceeds the value of 14 g/s (350 kHz), an additional increase in the erosion depth can be noticed. This could be due to the absorption of particle impact energy by the material through several mechanisms, such as microcracking, crack branching, crack arresting, etc. Thus, high-frequency loading (i.e. a high number of impacting particles) will be required to overcome these dissipation mechanisms. A very similar phenomenon was observed in Ref. [11] for HAE of refractory ceramics.

Fig. 4 shows the experimental results plotted against the depth values calculated with the brittle erosion model [6]. A reasonable agreement can be noticed for depths up to 70 mm. As this value is exceeded, the correlation drops drastically. A further striking feature is that concrete #1 does not fit the model at all over the entire parameter range. Concrete #2 behaves similarly but is showing good agreement for shallow cuts.

3.3. Acoustic emission measurements

Typical time domain AE-signals obtained for the mixtures #1 and #5 for identical experimental

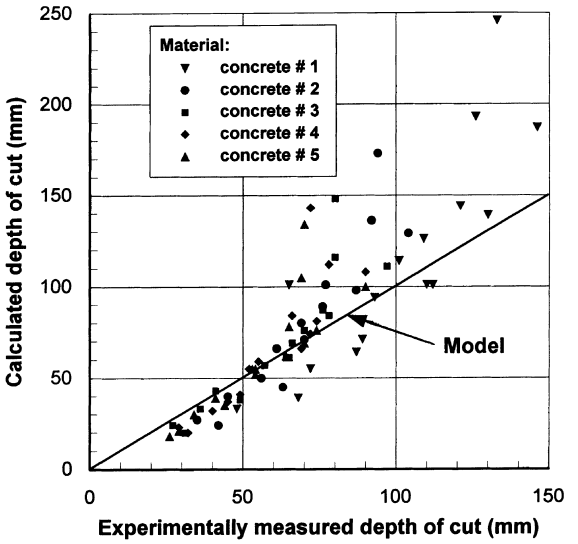

Fig. 4. Accuracy of the brittle erosion model for the investigated materials.

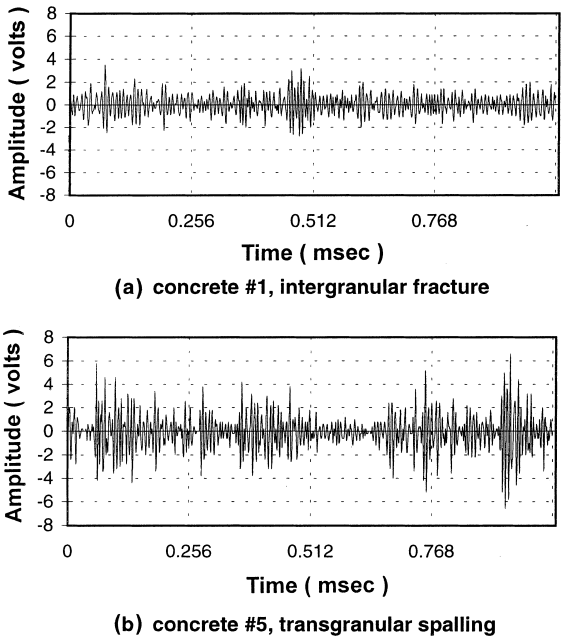

Fig. 5. Time domain AE-signals for two different concretes and photographs of wall structures showing different material removal modes. Experimental conditions: $v_A = 445$ m/s, $t_E = 0.32$ s, $\dot{m}_A = 7.41$ g/s): (a) Concrete #1, intergranular fracture; (b) concrete #5, transgranular spalling.

conditions are shown in Fig. 5. It can be noted that the AE-signal is predominantly of a continuous type for concrete #1 which is typical for a steady material removal mechanism; whereas, in the case of concrete #5, the AE-signal is primarily burst emission type which indicates the presence of unsteadily appearing energy sources. It can also be noticed that the signal peak-to-peak-amplitude is almost twice in the case of concrete #5 compared to concrete #1. The FFT of the time domain signals obtained for various process parameters are plotted in Figs. 6–8. The energy of the signal indicated by AE_{RMS} and the FFT-peak frequency as well as amplitude for various process parameters and different workpiece materials are given in Table 3.

The frequency domain AE-signals with change in the *abrasive particle velocity* for three concrete materials are plotted in Fig. 6. It can be seen that the amplitude of the FFT-signal increases with increasing particle velocity showing a trend similar to that of the erosion depth (Fig. 3(a)). There is a gradual reduction in the amplitude of the signal (acquired under the same conditions) from concrete #1 to #4, and an increase with concrete #5. In fact, the amplitude of the AE-signal is higher in concrete #5 than concrete #1. Concrete #5 is thus more sensitive to impact velocity variations compared to concrete #1, which could be due to different material removal modes. Given the same material removal modes (of concrete #1–#4), increase in the magnitude of the mechanical properties (Young's modulus, compressive strength, and absorbed fracture energy) causes decrease in the erosion depth and hence quantity of material removed. This leads to a drop in AE-signal amplitude.

The frequency domain AE-signals with change in *local exposure time* for three concrete materials are plotted in Fig. 7. It can be noted that the AE-signal generated in concrete #1 is much more sensitive to time variations than concrete #5. This matches the observations in Fig. 3(b) and could be attributed again to difference in material removal modes. There is an exponential increase in the amplitude of the AE-signal with increase in exposure time for concrete #1 which could be expected from the trend shown by the depth (Fig. 3(b)).

Table 3
AE_{RMS} and FFT-Peak of the AE-signalsfor various process parameters and materials

Cut No.	Concrete #1			Concrete #2			Concrete #3			Concrete #4			Concrete #5		
	AE_{RMS} (V)	FFT Peak		AE_{RMS} (V)	FFT Peak		AE_{RMS} (V)	FFT Peak		AE_{RMS} (V)	FFT Peak		AE_{RMS} (V)	FFT Peak	
		Freq. (kHz)	Ampl. (V)		Freq. (kHz)	Ampl. (V)		Freq. (kHz)	Ampl. (V)		Freq. (kHz)	Ampl. (V)		Freq. (kHz)	Ampl. (V)
1	0.4351	142.6	0.0959	0.4275	109.4	0.0864	0.1870	129.9	0.0490	0.3012	274.4	0.0703	0.6773	127.0	0.1495
2	0.4931	150.4	0.1115	0.7007	131.8	0.1585	0.3416	105.5	0.0855	0.3541	176.8	0.1094	0.8153	149.4	0.1682
3	0.6659	138.7	0.1531	0.7178	139.7	0.1441	0.5177	142.6	0.1523	0.3238	159.2	0.0656	1.0360	142.6	0.1969
4	0.8901	147.5	0.2240	0.7415	134.8	0.1521	0.5347	144.5	0.1328	0.3618	167.0	0.0734	1.2953	147.5	0.3771
5	1.0352	138.7	0.2250	0.8747	105.5	0.2043	0.5566	140.6	0.1367	0.4182	165.0	0.0641	1.3540	138.7	0.4609
6	1.1930	117.2	0.2951	0.9527	119.1	0.2755	0.5894	127.0	0.2330	0.4318	152.3	0.1031	1.4900	161.1	0.5031
7	1.9383	156.3	0.3805	1.0750	120.1	0.1192	1.1500	158.2	0.2734	0.1828	194.3	0.0347	0.6027	169.0	0.1414
8	0.4482	159.2	0.1004	0.4913	160.2	0.1356	0.6668	149.4	0.1400	0.2724	208.0	0.0470	0.4708	131.8	0.0891
9	NA	NA	NA	NA	NA	NA	0.5447	129.9	0.0864	0.1666	142.6	0.0370	0.3484	166.0	0.0566
10	0.1514	115.2	0.0371	0.4205	126.0	0.0951	0.4954	162.1	0.1242	NA	NA	NA	0.2300	146.5	0.0406
11	0.6719	137.7	0.1734	0.2714	127.9	0.0631	0.5606	137.7	0.1095	0.1848	180.7	0.0312	0.6105	123.1	0.1367
12	0.5997	164.6	0.1354	0.6132	102.5	0.1372	0.7152	130.9	0.1578	0.1364	193.4	0.0250	0.9135	143.6	0.1982
13	0.5748	113.3	0.1203	1.903	125.0	0.2724	0.6913	100.6	0.1543	0.1885	132.8	0.0352	0.8565	109.4	0.1941
14	0.5879	108.4	0.1354	0.4438	128.9	0.0775	0.7812	117.2	0.1697	0.4660	213.9	0.0722	1.1292	148.4	0.2520

Interestingly though, for the mixtures #2–#5 the increase in exposure time was leading to an increase in the AE-amplitude till an exposure time of $t_E = 0.32$ s and it reduced for the exposure time of $t_E = 0.635$ s. Visualization studies performed on the kerf geometries offer an explanation to this difference in trend. The results of these studies are discussed in Section 4.1. It may also be noted that there is a gradual reduction in the overall amplitude of the AE-signal from the mixtures #1 to #4, and then an increase for concrete #5. This trend is

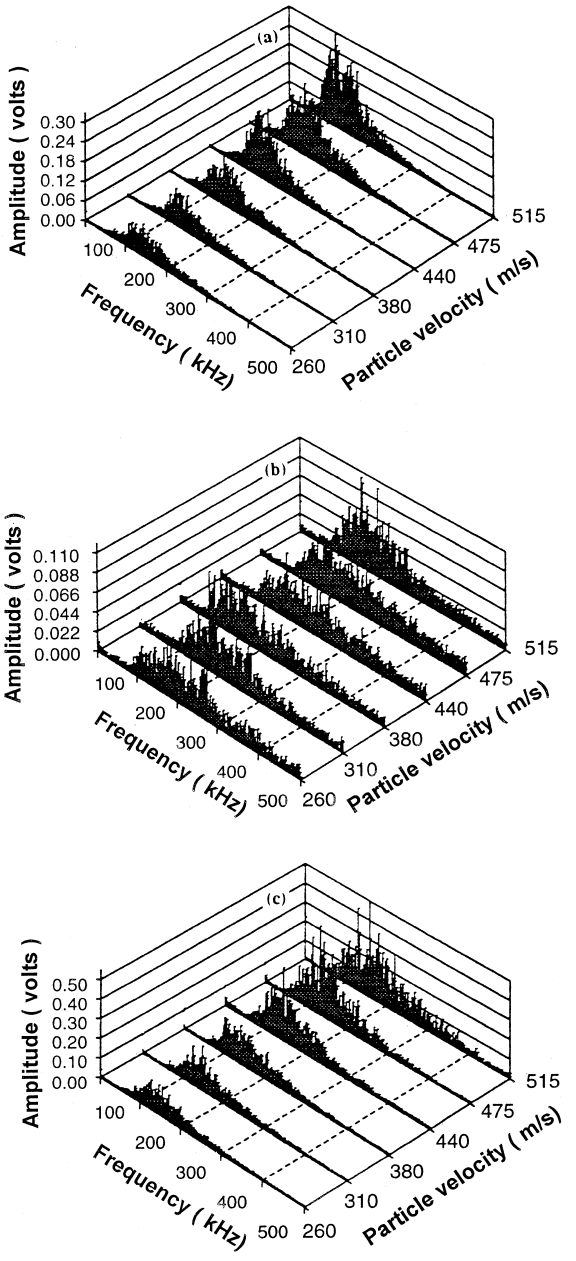

Fig. 6. Frequency domain AE-signals with change in abrasive particle velocity: (a) Concrete #1; (b) concrete #4; (c) concrete #5.

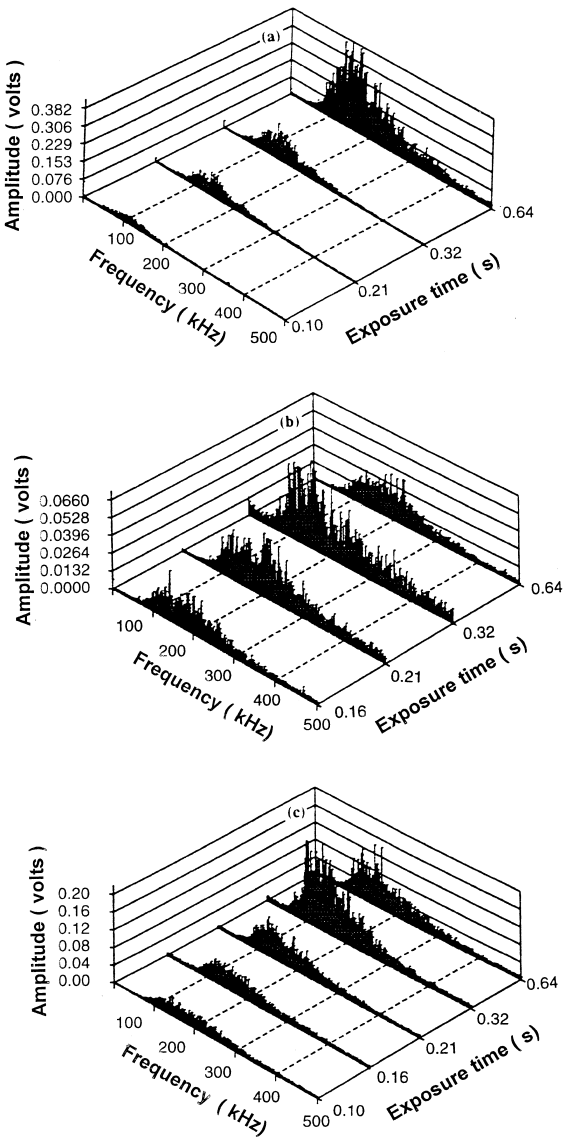

Fig. 7. Frequency domain AE-signals with change in local exposure time: (a) Concrete #1; (b) concrete #4; (c) concrete #5.

similar to that observed in the case of abrasive particle velocity variation.

The frequency domain AE-signals with change in *abrasive mass flow rate* for three concrete materials are plotted in Fig. 8. The overall amplitude of the frequency domain AE-signal drops gradually from concrete #1 to #4, and then increases with concrete #5. There is no appreciable trend observed in the amplitude of the AE-signal (similar to that of erosion depth) with increase in abrasive mass flow rate for any of the concrete materials. The causes for this behavior are discussed in Section 4.1.

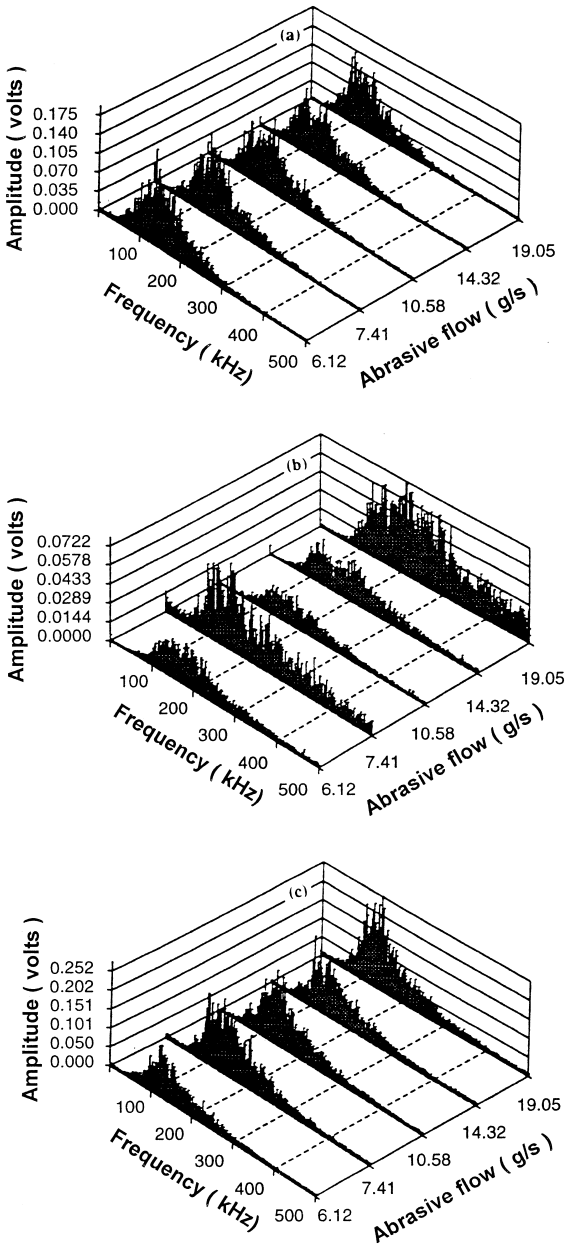

Fig. 8. Frequency domain AE-signals with change in abrasive mass flow rate: (a) Concrete #1; (b) concrete #4; (c) concrete #5.

3.4. Optical microscopy investigations

Results of the optical microscopy images taken from the upper parts of the erosion sites are shown in Fig. 9. Fig. 9(a) illustrates the structure of concrete #1 after it is eroded by HAE. It is clearly seen that the material is removed by inter-granular failure. Any cracks that have been activated, run through the weak interface between cement-matrix and aggregates. Several completely exposed grains are still visible. The locations where the aggregate particles are removed from, can also be seen. The same features can be observed in Fig. 9(b) illuminating the very similar failure behavior of concrete #2. The situation looks different in Fig. 9(c) that shows part of the erosion site of concrete #4. Here, a mixed mode between inter-granular failure and transgranular fracture can be detected. Whereas the left part of the photograph shows locations where inclusions have been exposed and removed completely, respectively, the right part exhibits inclusions that are partially broken. The transgranular fracture runs through the aggregate grains. The same observation can be made in Fig. 9(d) showing on its lower left part a very typical example of a large aggregate grain that is fractured. Additionally, microcracks are visible in the upper center and lower right area of the photograph, which could be a sign of crack arresting. As the crack went through an inclusion with high specific surface energy it might have got exhausted and could not run further. But in contrast to the images discussed previously, no undamaged, embedded or completely removed inclusion grains are visible in Fig. 9(d), indicating that the material failure is predominantly due to spalling fracture.

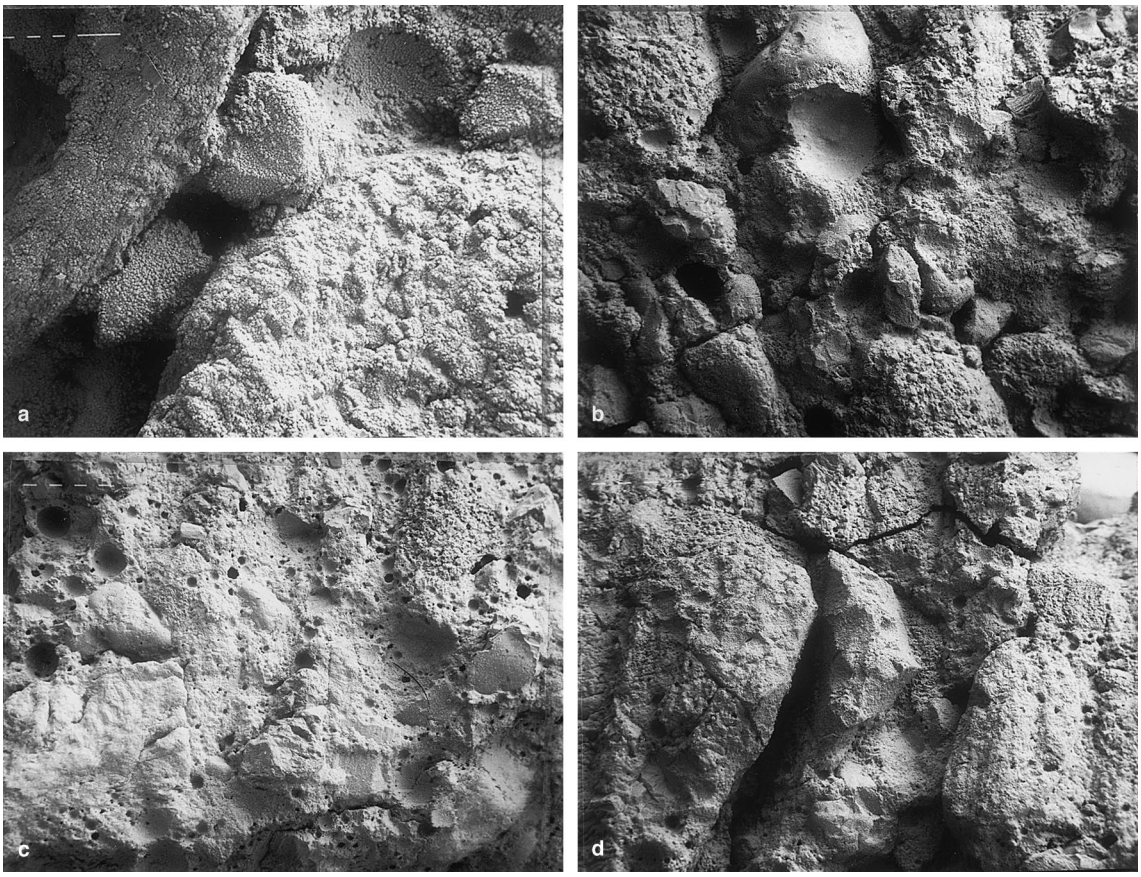

Fig. 9. Optical microscopy images from erosion sites: (a) Concrete #1; (b) concrete #2; (c) concrete #4; (d) concrete #5.

4. Discussion

4.1. Influence of process parameters on the AE signals

AE-signal acquired from the workpiece can be considered as a quantified measure of the kinetic energy dissipated on the erosion site with some damping effect (caused by turbulence of the high speed slurry), as suggested in Ref. [21]. The area enclosed by the FFT-curve or AE_{RMS} could be used for this purpose. The part of the kinetic energy dissipated in a cavity with the depth h is given [13] by

$$E_{DIS} = \chi(h)\frac{(\dot{m}_A + \dot{m}_w)}{2}(v_A - v_{THR})^2 t_E. \quad (5)$$

With increase in the *abrasive particle velocity* more kinetic energy is exposed to the workpiece material. Thus the higher amplitude of the AE-signal at higher velocities is an indication of the presence of a more powerful material removal process and larger amount of energy utilized for the erosion.

An increase in the *local exposure time* causes more energy to be dissipated at the cut. This leads to deeper cuts, more material removal, and hence higher amplitude for the AE-signal. Interestingly, the AE-signals for the mixtures #2–#5 show a slight decrease in amplitude at large exposure times. This may be an indicator of the onset of damping processes at the bottom of the cavity as discussed earlier and shown in Fig. 3(b). Although more energy is dissipated during the material removal process because of the longer exposure, the energy of the acquired signals seems to be reduced. As shown in Ref. [20] for AWJ cutting and in Ref.

[18] for solid particle erosion, a fluid film on the surface of eroded material can dampen AE-signals. This drop in the AE-signal was not observed on concrete #1 (see Fig. 7(a)) indicating that this material mixture was not sensitive to damping effects. In fact, large cavities were observed in the kerfs of concrete #1 caused by intense washing out of the hardened cement matrix. This effect is shown in Fig. 10(a). These cavities created additional space for the abrasive–water mixture to escape and probably prevented significant damping effects. In contrast, as shown in Fig. 10(b), the cuts in the high-strength materials do not show these large cavities. Therefore, the kerf walls of these materials may restrict the high-speed slurry in the kerf which creates the damping effects. These relations are in agreement with the results from the erosion depth measurements (Fig. 3(b)) as it was found that the initial progress of the time-function is extraordinarily high for concrete #1 indicating a reduced damping effect.

The influence of the *abrasive mass flow rate* on the AE-signal characteristics is not very significant. This observation is in agreement with Fig. 3(c) which shows that the abrasive mass flow rate has just a minor influence on the erosion depth in the investigated range. As the abrasive mass flow rate is much lower than the water mass flow rate (in this study: $\dot{m}_A/\dot{m}_w \approx 0.1$), Eq. (5) indicates that variations in the abrasive mass flow rate will not change the dissipated energy significantly. The increase in the integral abrasive particle mass and thus of the higher impact frequency, due to the higher abrasive mass flow will be compensated by the decrease in the mean particle velocity (Eq. (2)). Therefore, the AE-signals in Fig. 8 are an indicative of real conditions.

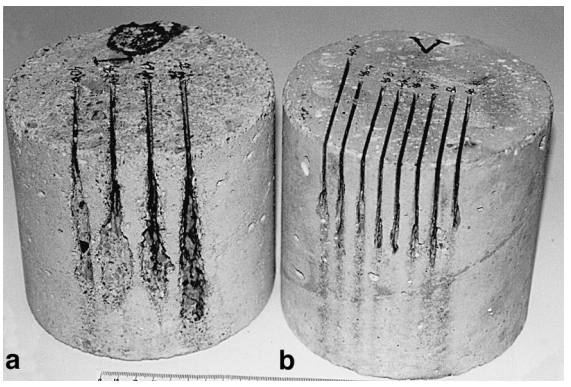

Fig. 10. Visualization of kerf geometries indicating different material removal mechanisms: (a) Concrete #1, large cavities in the lower range; (b) Concrete #5, comparatively straight kerfs.

4.2. Influence of material properties on the AE-signals

Figs. 5–10 and Table 3 contain information on the influence of the material properties on the detected AE-signals. Based on the assumption that the energy of the AE-signals are related to the energy dissipated during the material removal process [21], it may be ingenious to discuss the influence of the energy absorbed during the compression test on the structure of the measured AE-signals.

The relation between the AE_{RMS} and the energy absorbed during the compression test is shown in Fig. 11. The AE_{RMS} corresponding to different process parameters are indicated by the points. Two trends could be noticed from these figure. First, the AE_{RMS} generally reduce with increase in the mechanical properties of the materials. Second, the magnitude of AE_{RMS} for concrete #5 is comparatively high.

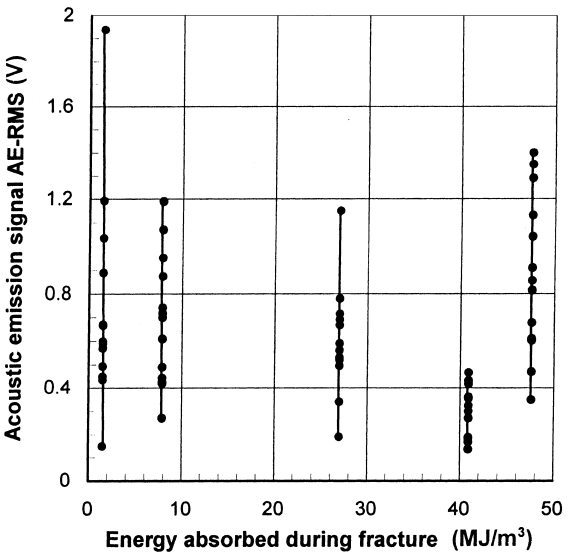

Fig. 11. Relation between absorbed fracture energy and AE_{RMS}.

The first trend could be explained by the observations made in the previous chapter. There, it was found that the intensity of the AE-signals generally decreases with a drop in the energy dissipated during the material removal process. With increasing absorbed fracture energy, less material is removed from the workpiece. The material removal mechanisms at the erosion site can be investigated through AE-visualization studies of the specimens. The HAE signals from the wall structure for two concrete mixtures are shown in Fig. 5. The structures for concrete #2–#4 are similar to that of concrete #1. Fig. 5(a) clearly shows that the material in concrete #1 is removed by HAE due to intergranular erosion mechanism which is characterized by high degree of undamaged aggregate grains. The failure path is along the interface between aggregate grain and hardened cement matrix. The matrix is removed separately which could be due to the action of the high velocity water flow. These assumptions are also supported by observations made on the compressive test specimens (see Fig. 2(a)) and the macro-geometry of the erosion site (see Fig. 10(a)) as described earlier as well as by microscopic investigations on the specimens (Fig. 9(a)). The material failure is almost 100% inter-granular for concrete #1. Although the amount of intergranular erosion decreases with the absorbed fracture energy of the eroded materials (see Fig. 9), it dominates the material removal mechanism at least for the mixtures #1–#4. Assuming a fairly identical uniform material removal mode for these concrete mixtures, less energy is dissipated during the erosion process in the samples with higher strength properties which leads to a drop in the AE_{RMS} and also in the FFT-peak. In contrast, the AE-structure shown in Fig. 5(b) clearly illustrates that material failure in mixture #5 is primarily due to trans-granular fracture; there is an inclusion fracture of almost 100%. This is most probably due to the homogenization of the structure. Since the cement matrix is comparatively hard and the inclusion grains are large, the structure in general is more homogeneous. This homogenization effect becomes active as the material is subjected to high stress rates. During the material removal process, cracks run preferably through the aggregate grains. Although this mechanism may shorten the path of the cracks as there is no crack deflection or crack branching, the aggregate grains absorb a high amount of energy for fracture. Typically, the specific surface energy of the aggregate material is one order of magnitude higher than the specific surface energy of the interface between aggregate and hardened cement paste [25]. As the differences in the erosion depths between the specimens #4 and #5 are not very large, the effects of accelerated energy dissipation due to the aggregate fracture may explain the increase in the AE-signal intensity in the concrete material #5. The type of the time domain AE-signal also provides a clue to the presence of different material removal mechanisms. Whereas the AE-signal for the concrete #1 (Fig. 5(a)) shows a fairly continuous behavior, the AE-signal of the concrete #5 (Fig. 5(b)) is characterized by burst emissions, illustrating the sudden energy release, most probably due to the spalling fracture of the structural elements.

Thus, the AE-signals seem to be sensitive to changes in the material removal regime during HAE. Probably, the regions of minimum AE-signal intensity in Fig. 11 indicate a transition range between a granular erosive material removal mode and a spalling fracture mode.

The different failure behavior of concrete #1 as discovered by the AE-studies is further illustrated in Fig. 4. The large deviations of the measured depths from the model line suggest that the mechanism of crack-network generation, that is suggested in Ref. [6], as a result of stress waves induced by impacting abrasive particles, is not valid for concrete #1. There is strong evidence to suggest that the erosion of this material type is supported by action of high-speed water flow in the eroded kerf. This flow will wash the very weak matrix away and the undamaged inclusion grains will then be separated. As this additional erosive mechanism is not considered in the model, the calculation procedure for concrete #1 fails.

5. Summary and conclusions

Acoustic emission measurements on pre-cracked multiphase materials indicate that AE-sensing technique is a promising tool to identify on-line the different material removal mechanisms

occurring during HAE. Material removal dominated by intergranular fracture is typically characterized by a continuous type of AE-signal; whereas material removal dominated by transgranular fracture is characterized by burst emissions illustrating the sudden energy release during inclusion fracture.

The results obtained from the compression tests indicate that with increase in mechanical strength properties of pre-cracked multiphase materials, the failure mode changes from 'crumble' intergranular fracture for low strength materials to a 'spalling' transgranular fracture for high-strength materials. This is also true for HAE. The AE-signal is capable of identifying this trend very effectively.

Any change in process parameter which increases the erosion depth and quantity of removed material, causes the energy dissipated in workpiece material to increase. AE-signal is capable of detecting this change in the energy dissipated in the materials and hence AE_{RMS} can be used as a quantitative measure of this dissipated energy. However, at large exposure times the damping effect of the erosive slurry on the erosion reduces the AE-signal amplitude in brittle materials which are characterized by spalling trans-granular fracture.

Nomenclature

A	regression parameter
AE_{RMS}	RMS of the acoustic emission signal
d_F	focus diameter
E_{AB}	energy absorbed during compressive testing
E_{DIS}	energy dissipated during erosion process
h	cutting (erosion) depth
m_A	abrasive mass flow rate
m_w	water mass flow rate
p	pump pressure
R_s	thermal shock resistance
t_E	local exposure time
t_{THR}	incubation time
v_A	abrasive particle velocity
v_T	traverse rate
v_{THR}	threshold abrasive particle velocity
v_W	water jet velocity
Y_M	Young's modulus
ε	strain
ε_{ult}	ultimate strain
$\chi(h)$	energy dissipation function
ϕ	momentum transfer coefficient
μ	momentum transfer coefficient
ρ_M	target material density
ρ_w	water density
σ_M	compressive strength
σ_{ult}	ultimate stress

Acknowledgements

The authors are thankful to the Alexander von Humboldt Foundation, Bonn, Germany, for the financial support.

References

[1] T.J. Kim, G. Sylvia, L. Posner, Piercing and cutting of ceramics by abrasive waterjet, PED-vol. 17, ASME, New York, 1985, pp. 19–24.
[2] K.F. Neusen, P.K. Rohatgi, D. Alberts, Abrasive waterjet cutting of metal matrix composites, in: Proceedings of the Fourth US Water Jet Conference, ASME, New York, 1987, pp. 175–182.
[3] B. Freist, H. Haferkamp, A. Laurinat, H. Louis, Abrasive jet machining of ceramic products, in: Proceedings of the Fifth American Water Jet Conference, Water Jet Technology Association, St. Louis, 1989, pp. 191–204.
[4] G. Hamatani, M. Ramulu, Machinability of high temperature composites by abrasive waterjet, Trans. ASME J. Engng. Mat. Technol. 112 (1990) 381–386.
[5] J. Zeng, T.J. Kim, Material removal of polycrystalline ceramics by a high-pressure abrasive water jet – a SEM study, Int. J. Water Jet Technol. 1 (1991) 65–71.
[6] J. Zeng, T.J. Kim, Development of an abrasive waterjet kerf cutting model for brittle materials, Jet Cutting Technology, Kluwer Academic Publication, Dordrecht, 1992, pp. 483–501.
[7] A.W. Momber, R. Kovacevic, Principles of Abrasive Water Jet Machining, Springer, London, 1998.
[8] M. Ramulu, S.P. Raju, H. Inoue, J. Zeng, Hydro-abrasive erosion characteristics of 30vol.% SiC_P 6061-T6 Al composite at shallow impact angles, Wear 166 (1993) 55–63.
[9] L. Kahlman, S. Karlsson, R. Carlsson, C.G. Nilsson, Wear and machining of engineering ceramics by abrasive waterjets, Amer. Ceram. Soc. Bull. 72 (1993) 93–98.
[10] H. Hochheng, K.R. Cheng, Material removal analysis in abrasive waterjet cutting of ceramic plates, J. Mat. Proc. Technol. 40 (1994) 287–304.

[11] A.W. Momber, I. Eusch, R. Kovacevic, Machining refractory ceramics with abrasive water jets, J. Mat. Sci. 31 (1996) 6485–6493.
[12] S.P. Raju, M. Ramulu, Predicting hydro-abrasive erosion wear during abrasive water jet cutting, in: Manufact. Science and Engineering, vol. 1, ASME, New York, 1994, pp. 339–351.
[13] A.W. Momber, R. Kovacevic, Quantification of energy absorption capability in abrasive water jet machining, J. Engng. Manufact. 209 (1995) 491–498.
[14] A. Momber, R. Kovacevic, Test parameters analysis in abrasive water jet cutting of rocklike materials, Int. J. Rock Mech. Min. Sci. 34 (1997) 17–25.
[15] M. Ramulu, Dynamic photoelastic investigation in the mechanics of waterjet and abrasive waterjet machining, Optics and Lasers in Eng. 19 (1993) 43–65.
[16] R. Kovacevic, R. Mohan, Y.M. Zhang, Cutting force dynamics as a tool for surface profile monitoring in AWJ, Trans. ASME J. Eng. Ind. 117 (1995) 340–350.
[17] T. Okamura, R. Oshima, K. Satoh, J. Sato, Erosion intensity of submerged cavitating jets, in: Proceedings of the 9th International Symposium on Jet Cutting Technology, BHRA Fluid Engng., Cranfield, 1988, pp. 33–48.
[18] W. Hübner, E. Leitel, A. Rolle, J. Lehmann, G. Bülow, Schallemissionsanalyse erfasst Feststoffteilchen-Einschläge, Materialprüfung 34 (1992) 13–16.
[19] R.A. Tikhomirov, V.F. Babanin, E.N. Pethukov, I.D. Starikov, V.A. Kovalev, Gidrorezanje Sudostroitel'nikh Materialov, Sudostroenie, Leningrad, 1987.
[20] R. Mohan, A.W. Momber, R. Kovacevic, On-line monitoring of depth of AWJ penetration using acoustic emission technique, Jet Cutting Technol., Mech. Engng. Publ. Ltd., London, 1994, pp. 649–664.
[21] R. Mohan, A. Momber, R. Kovacevic, Detection of energy absorption during abrasive water jet machining using acoustic emission, MED-vol. 2-1, ASME, New York, 1995, pp. 69–85.
[22] A.W. Momber, R. Kovacevic, Energy dissipative processes in high-speed water solid-particle erosion. HDT-vol. 231/FED-Vol. 233, ASME, New York, 1995, pp. 243–256.
[23] A.W. Momber, The fragmentation of standard cylinders during the compressive testing, Lett. Fracture Micromech. 74 (1998), in press.
[24] A.G. Evans, M.E. Gulden, M. Rosenblatt, Impact damage in brittle materials in the elastic-plastic response regime, Proc. Roy. Soc. Lond. A 361 (1978) 343–365.
[25] S. Ziegeldorf, Fracture mechanics parameters of hardened cement paste, aggregates, and interfaces, in: Fracture Mechanics of Concrete, Elsevier, Amsterdam, 1983, pp. 371–409.